Tailoring the Local Conductivity of TiO2 by X-Ray Nanobeam Irradiation

Tailoring the Local Conductivity of TiO_2 by X-ray Nanobeam Irradiation

Lorenzo Mino,[1*] Valentina Bonino,[2] Federico Picollo,[2] Matteo Fretto,[3] Angelo Agostino,[1,4] Marco Truccato[2,4]

[1]Department of Chemistry, Interdepartmental Centre NIS, University of Torino, via Giuria 7, 10125 Torino, Italy.
[2]Department of Physics, Interdepartmental Centre NIS, University of Torino, via Giuria 1, 10125 Torino, Italy.
[3]Nanofacility Piemonte INRiM (Istituto Nazionale di Ricerca Metrologica), Strada delle Cacce 91, 10135 Torino, Italy.
[4]CrisDi Interdepartmental Center for Crystallography, University of Torino, Torino, Italy.
*Corresponding Author e-mail: lorenzo.mino@unito.it

Graphical Table of Contents

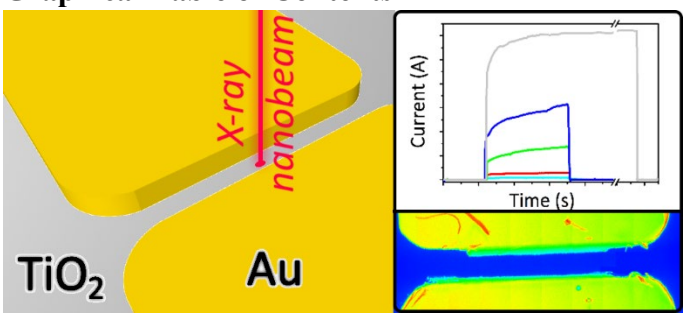

A synchrotron X-ray nanobeam to directly write conductive channels of oxygen vacancies with sub-micrometer dimension on TiO_2 crystals is employed. This X-ray nanopatterning process is based on the modification of the local oxygen content and can represent a promising tool for the nanofabrication of oxides, tuning the material resistivity. X-ray nanopatterning could enable the production of new memristive devices.

Abstract

It is well known that intense synchrotron beams can alter the state of materials, but this effect is generally considered undesired radiation damage. However, intriguing phenomena, which enable to modify materials in a controlled way, have been recently reported. We investigated the effect of local irradiation of TiO_2 rutile single crystals by a 56×57 nm^2 synchrotron X-ray nanobeam at 17.4 keV. Besides a transient increase of conductivity due to a photovoltaic-like process, we measured a non-volatile localized change of resistance by about 4 orders of magnitude after X-ray exposure. This effect can be ascribed to the local generation of oxygen vacancies by the X-ray nanoprobe, which are subsequently ordered by the electric field applied during the acquisition of

I-V curves. Our results demonstrate that intense synchrotron beams can create oxygen vacancies in materials with tightly bound oxygen atoms, highlighting that X-ray nano-probes could become an effective tool for oxide nano-fabrication, able to locally tune the material resistivity. For instance, since the localized presence and migration of oxygen vacancies is an essential requisite for redox-based memristive devices, the possibility to locally induce oxygen vacancies could represent a novel tool for the production of oxide-based memristive devices, replacing the problematic electroforming step.

1. Introduction

It has long been known that intense synchrotron X-ray beams can alter the state of matter.[1] This issue has been widely studied in the field of soft matter and protein crystallography since radiation damage is a major concern in experiments involving these systems.[2] Inorganic hard condensed matter is generally much less sensitive to X-rays, nevertheless the recent remarkable improvements in both brilliance of synchrotron radiation sources and performance of X-ray focusing optics are pushing the power density on the sample to unprecedented values in nanobeam experiments,[3] making radiation damage relevant also for inorganic materials.[4] However, in the last years some studies suggested that this effect, which is generally undesired, could be exploited to modify materials in a controlled way. In this respect, a few interesting examples have been reported, including for instance redox reactions,[5] X-ray induced crystallization,[6] metal-insulator[7] and structural phase transitions.[4a, 8]

In the case of the non-stoichiometric superconducting oxides, Poccia *et al.*[9] showed that 12.4 keV X-rays can induce the ordering of interstitial O atoms and a change in the critical temperature of La_2CuO_{4+y}. Thereafter our group highlighted that a high-dose irradiation at 17 keV can affect both structural and electronic properties of $Bi_2Sr_2CaCu_2O_{8+\delta}$ (Bi-2212) micro-crystals by modifying both their mosaicity and their oxygen content (i.e. displacing weakly bound interstitial O atoms and thus increasing the material resistivity).[10] Taking inspiration from these

results, we have developed the idea of exploiting synchrotron radiation to directly write the geometry of an electrical device on the material without any additional step, like photoresist impression and subsequent etching, as done in conventional lithographic processes. This X-ray nanopatterning (XNP) process is based on the modification of the material oxygen content (and thus of its local electrical properties) induced by the X-ray nanobeam. Following this approach, we succeeded in fabricating a proof-of-concept Josephson device out of Bi-2212 without disrupting its crystal structure using XNP,[11] recently achieving a minimum feature size of 50 nm.[12]

On the other hand, a lot of efforts is presently being spent in the field of oxide electronics, where many full-oxide electronic components have already been fabricated, up to monolithically integrated circuits.[13] The typical patterning process used for these fabrications has been ordinary electron-beam or photo-lithography, borrowing the technology widely used for semiconductors. Some studies also employed UV irradiation to induce local metallic states in the oxide.[14] Although in principle XNP could be applied to all oxide materials, so far it has been tested only on non-stoichiometric superconducting oxides, which feature loosely bound oxygen atoms. However, a recent study highlighted that prolonged X-ray irradiation, combined with the simultaneous application of an electric field, can induce non-volatile resistance changes in Pt/TiO_2/Pt cells.[15] Although no control on the spatial distribution of the conducting regions was achieved in these experiments, these results suggest that intense synchrotron beams can create oxygen vacancies also in materials with more tightly bound oxygens atoms, indicating the possible extension of the XNP process to the whole class of functional oxide materials.

The XNP process would be especially interesting in the case of redox-based memristive devices, one of the most attractive emerging memory technologies, since the ability to induce the localized

presence of oxygen vacancies in transition metal oxides represents an essential requirement for their fabrication.[16] Indeed, the operation principle of these devices is based on a reversible resistance change of the dielectric layer (e.g. TiO_2, $SrTiO_3$, HfO_2, TaO_x) in a simple capacitor structure.[17] This resistance change is a result of voltage-driven migration of oxygen vacancies, which act as mobile donors. After a so-called electroforming step, which creates oxygen vacancy channels (the "filaments") in an insulating matrix within the dielectric, the device resistance can be switched between a high resistance state and a low resistance state.[18] Unfortunately, the electroforming step is highly undesirable because of CMOS-incompatible high voltages and the time-consuming necessity of addressing every individual cell on a chip prior to operation. In addition, the stochastic nature of the electroforming process induces a significant device-to-device variation.[19] In principle, XNP, if applicable to the metal oxides used in memristive devices, could potentially overcome these issues. Therefore, the present paper is devoted to explore the possibility of extending the use of XNP to a typical, widely-used functional oxide like TiO_2.

2. Results and Discussion

To investigate the effect of X-ray nanobeam irradiation on the oxide electrical properties, we deposited Au electrical contacts on the TiO_2 rutile single crystals by physical vapour deposition (see Figure 1 and Experimental section). The gap between each couple of Au contacts was 5 μm: this region was modified by X-ray nanopatterning (Figure 1d). The chips were mounted on a customized sample holder (Figure 1a-b), allowing two-probe electrical measurement in the ESRF ID16B-NA nanobeam setup, to monitor *in situ* the variations in the sample electrical conductivity during the irradiation. After a preliminary alignment using an optical microscope, the region of interest in the sample was precisely located by X-ray fluorescence (XRF) maps.

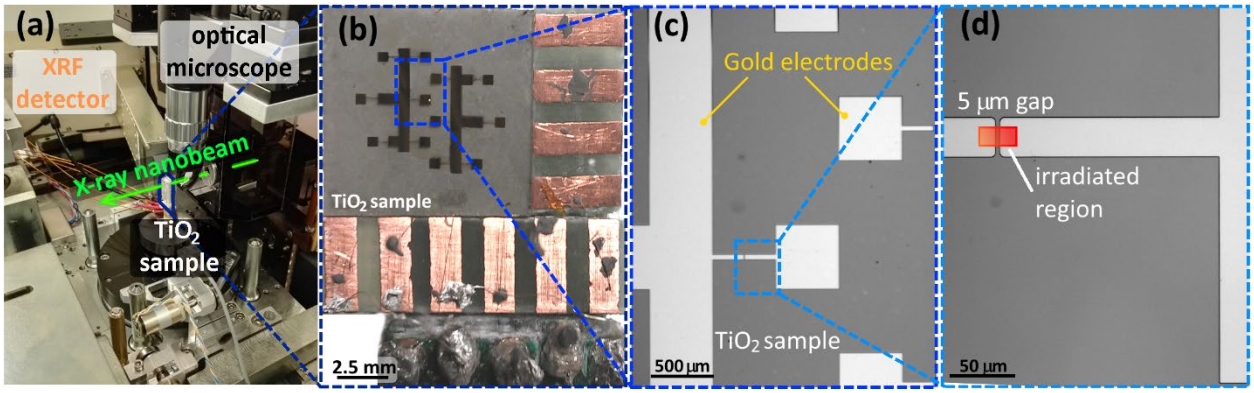

Figure 1. (a) Photograph of the experimental setup employed at the ESRF ID16B-NA beamline showing the alignment optical microscope, the XRF detector and the sample holder used for the online electrical measurements (b) TiO_2 sample mounted on the sample holder employed for online electrical characterization. (c) Optical micrograph of the Au contacts deposited on the TiO_2 single crystal for electrical characterization. (d) Magnification of the 5 µm gap between two Au electrodes employed to perform the X-ray irradiation procedures.

As a first step of our study, we investigated the effect of irradiating with an increasing photon flux a single point in the 5 µm gap between a couple of Au electrodes using a 56 × 57 nm^2 nanobeam at 17.4 keV. Figure 2 shows the time-dependent current level at 1 V: the initial value in dark conditions is in the order of 10^{-12} A. When the shutter of the X-ray beam is opened, we can observe an increase of the current proportional to the incident photon flux reaching a maximum of ~ 6 × 10^{-9} A for a flux of 6.7 × 10^{10} ph s^{-1}. As soon as the shutter is closed, the resistance goes back to the initial value within a few seconds, even for long irradiation times (up to 25 minutes) at the maximum photon flux (see grey curve in Figure 2). Also comparing the I-V curves of the sample before and after X-ray exposure no evident changes are present (see Figure S1 in the Supporting Information).

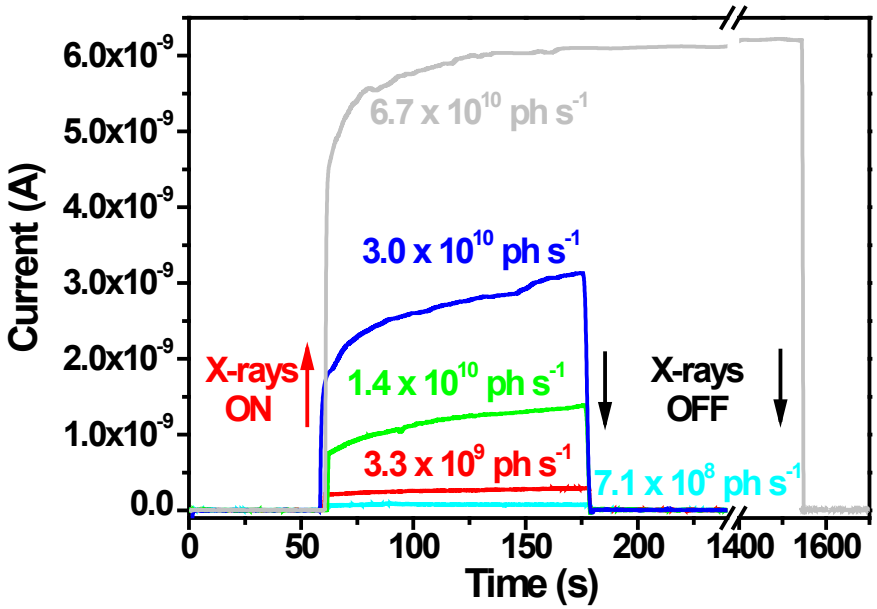

Figure 2. Time-dependent current change for X-ray irradiation of a single point between two Au electrodes for different photon fluxes. A constant bias of 1 V was set during the measurement. The shutter of the X-ray nanobeam was opened at 60 s and closed at 180 s in all cases, except for the maximum flux in which was closed at 1550 s.

As shown in Figure 3a, the point which has been irradiated can be localized using a scanning electron microscope (SEM). A more detailed investigation was then performed using atomic force microscopy (AFM): topographic maps highlighted a local increase in the height of the crystal induced by the long exposure to the synchrotron nanobeam, reaching a maximum of about 90 nm (Figure 3b). However, conductive atomic force microscopy (C-AFM) maps (Figure 3c) did not show evident differences in the local conductive properties of the TiO_2 crystal with respect to pristine samples (see Figure S2 in the Supporting Information). Indeed, a measurable current is flowing only when the AFM tip is in contact with the bottom Au electrode, which is biased during the measurements. These data imply that no conducting channel has been originated between the two electrodes, in agreement with the electrical behaviour observed after X-ray irradiation (Figures 2 and S1).

Therefore, these results suggest that for single point irradiation the current increase is essentially due to a volatile photovoltaic-like process. Since Au has a higher work function than TiO_2, in dark conditions an electron transfer from TiO_2 to Au occurs until a thermodynamic equilibrium is reached by forming a depletion layer (i.e. a Schottky barrier) at the Au/TiO_2 interface.[20] When the sample is under X-ray irradiation, the photogenerated electrons can cause a shift of the TiO_2 Fermi level to a new quasi-Fermi level, associated to an electron transfer from TiO_2 to the Au electrode before electron/hole recombination.[21] The system gradually approaches a new nonequilibrium illumination condition, in which the current flow is determined by the applied electric field and by the X-ray intensity (see Figure 2). After stopping the irradiation, the pristine thermodynamic equilibrium in dark conditions is restored.

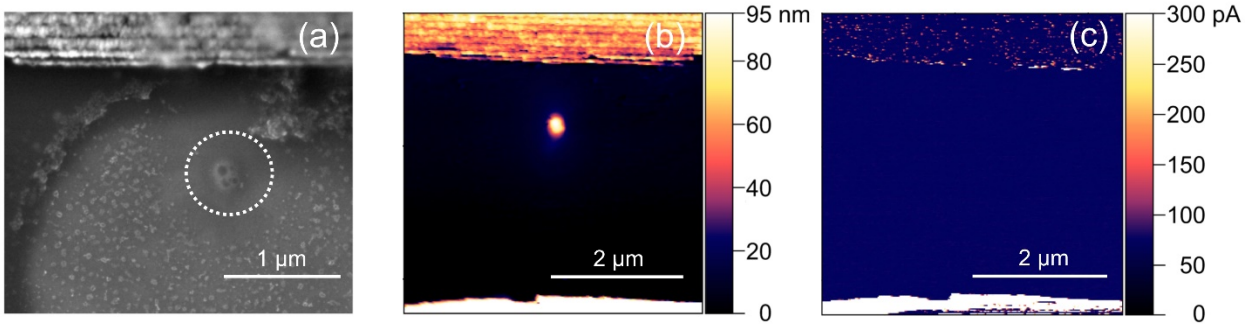

Figure 3. SEM image (a), topographic AFM (b) and current C-AFM (c) maps of the TiO_2 single crystal after 25 minutes of X-ray nanobeam irradiation at the maximum photon flux (6.7×10^{10} ph s^{-1}) in a single point between the two Au electrodes. The dotted white circle in part (a) highlights the irradiation point.

The second experiment was devoted to the realization of a single irradiation line connecting two Au electrodes. The irradiation started at the center of the edge of one Au contact and arrived till the edge of the other contact using a step of 50 nm and an irradiation time of 1 s per point. The same spatial line was irradiated 5 times at increasing beam intensities and I-V curves were acquired a few minutes after each X-ray exposure. From the inset of Figure 4, we can see that at low photon

fluxes (< 10^{10} ph/s) there are no evident changes in the electrical properties of the sample after each irradiation step. Conversely, for high photon fluxes we can observe a progressive increase of the current flowing during the acquisition of the I-V characteristics (Figure 4). From the SEM image (Figure 5a), XRF map (Figure 5b) and topographic AFM map (Figure 5c) of the irradiated area, we cannot see evident sample modifications. However, a clear change of the local conductive properties with respect to pristine samples is appreciable in the C-AFM map reported in Figure 5d. Indeed, a measurable current is flowing also when the AFM tip is in contact with the top Au electrode, which is not electrically wired, suggesting the presence of conductive channels in the TiO_2 crystal.

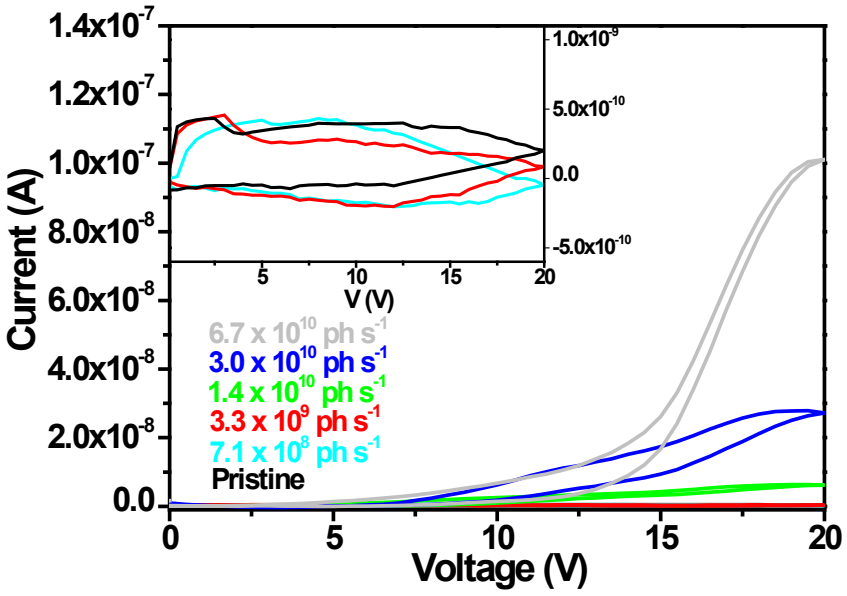

Figure 4. I-V curves of the TiO_2 single crystal acquired after each irradiation line between two Au electrodes at increasing X-ray photon fluxes. In the inset a magnification of the I-V curves for the irradiation at low photon fluxes is reported.

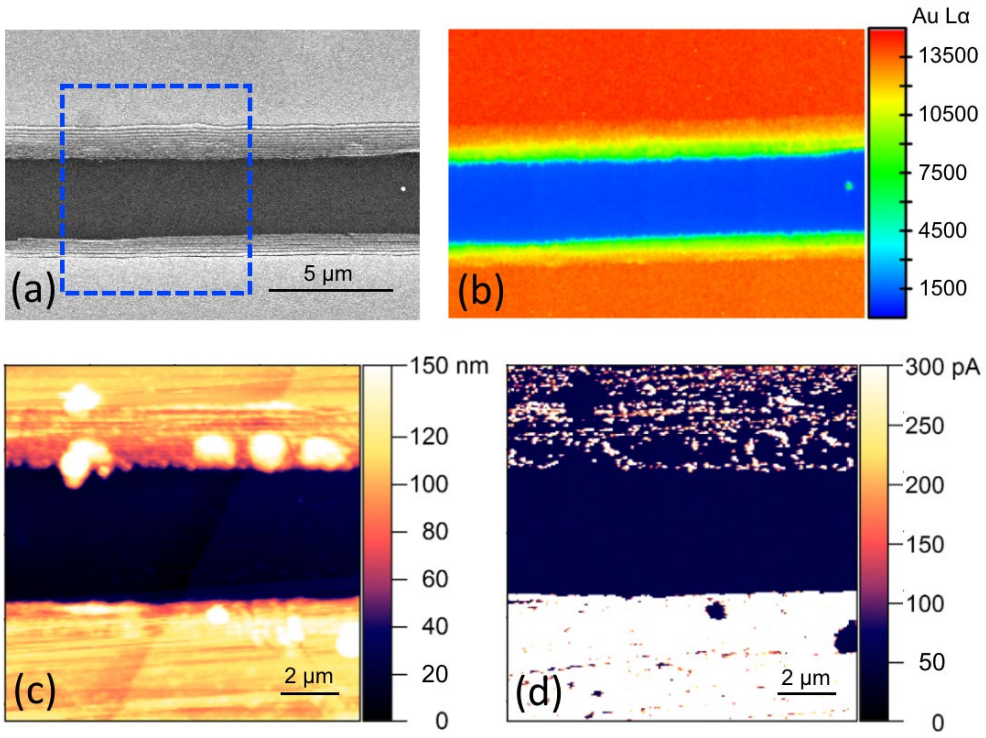

Figure 5. SEM image (a), Au Lα XRF (b), topographic AFM (c) and current C-AFM (d) maps of the area in which the irradiation line between two Au electrodes has been realized. These maps were acquired after all the irradiation steps at increasing X-ray photon fluxes reported in Figure 4. The blue dashed box in the SEM image highlights the area in which the AFM maps were acquired.

An even more pronounced effect can be obtained by repeatedly irradiating a line connecting two Au electrodes using the maximum photon flux. Indeed, after four X-ray irradiations (1IR, 2IR, 3IR and 4IR) on the same line at the maximum photon flux, the sample conductivity increases by about 4 orders of magnitude with respect to the pristine TiO_2 crystals (Figure 6). In this case the irradiated line can be easily recognized also in SEM images (Figure 7a). Topographic AFM maps (Figure 7b) show a slight crystal expansion, limited to less than 10 nm, which is more evident looking to the maps reporting the AFM deflection signal (Figure 7d). Moreover, the C-AFM maps (Figure 7c) show a huge enhancement in the current flowing when the AFM tip is in contact with the top Au electrode, which becomes comparable to the current measured on the biased bottom Au electrode. Nevertheless, also in these conditions no evident changes in surface conductivity can be

highlighted on the irradiated TiO_2, suggesting that the conductive channels formed in the TiO_2 crystal are sub-superficial.

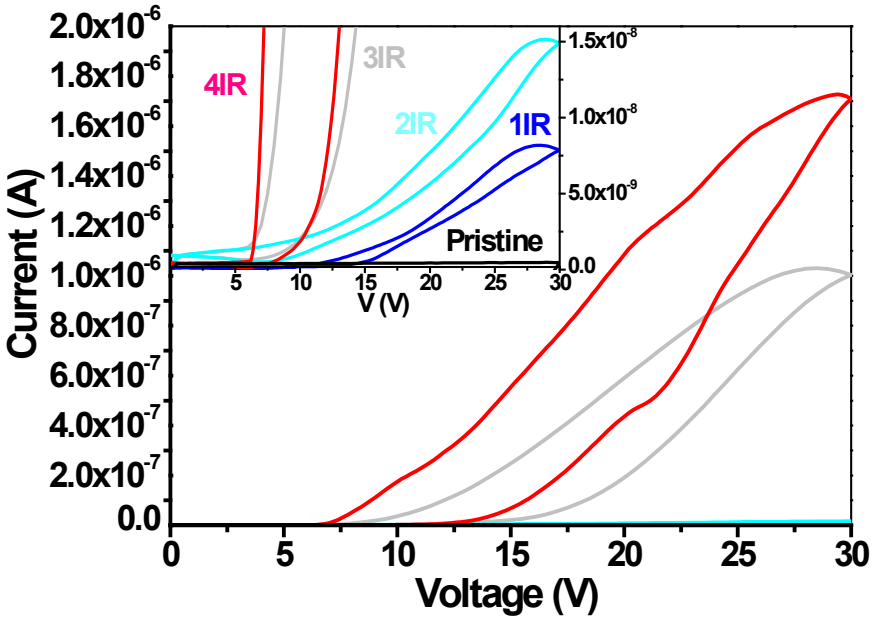

Figure 6. I-V curves acquired after each of the four X-ray irradiation steps (1IR, 2IR, 3IR and 4IR) on an irradiation line between two Au electrodes at the maximum photon flux (6.7×10^{10} ph s^{-1}).

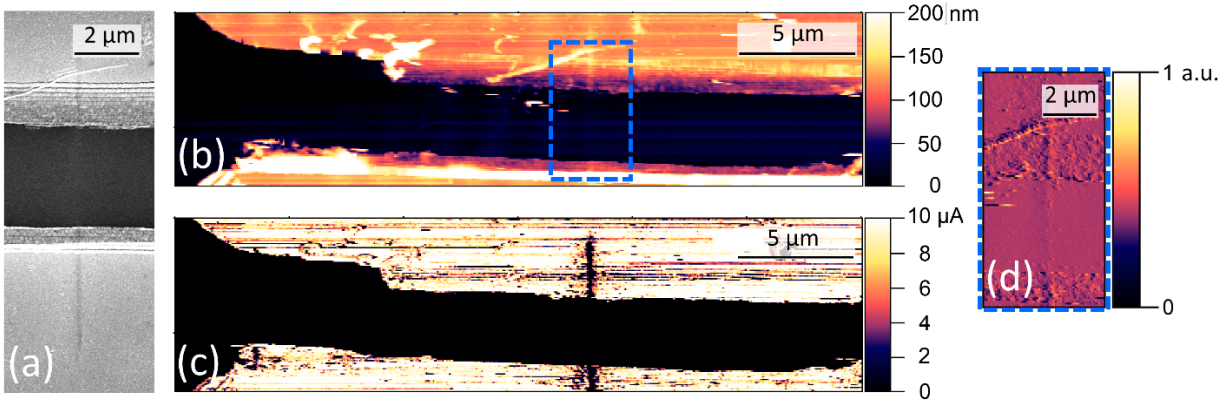

Figure 7. SEM image (a), topographic AFM (b) and current C-AFM (c) maps of the TiO_2 single crystal after four X-ray doses (1IR, 2IR, 3IR and 4IR) on an irradiation line between two Au electrodes at the maximum photon flux (6.7×10^{10} ph s^{-1}). Part (d) reports the AFM deflection signal for the regionhighlighted by the blue dashed box in part (b), which includes the vertical irradiation line.

All these observations show that, besides the volatile photovoltaic-like processes described above, X-ray nanobeam irradiation can induce non-volatile changes in the TiO_2 local electrical properties. This behaviour can be explained by considering that X-ray irradiation can create defects in transition metal oxides.[4a, 9, 22] Indeed, after absorption of a X-ray photon and emission of a photoelectron, in the fs timescale the excited atom undergoes a de-excitation process resulting in the emission of a fluorescence photon or of an Auger electron (more probable in low Z atoms).[4b, 23] The secondary and Auger electrons generate electron/hole pairs during their transport in the material being involved in knock-on and bond breaking processes.[1, 10c, 24] Previous Monte Carlo simulations on other oxide materials showed that the secondary electrons generated by the X-ray nanobeam can influence the material properties a few hundred of nanometers around the irradiation point.[10c] Moreover, at very high dose rates, the lack of enough conduction electrons in insulating materials can prevent the quick reinstatement of the local electrical neutrality and the Coulomb repulsion between positive charges may induce ion ejection. [24-25] It is worth noting that in our experiment the maximum irradiance was 6×10^{10} W m^{-2}, considerably higher than in other studies that observed similar effects over much longer timescales.[15]

All the processes described above can cause bond breaking and defect formation, especially oxygen vacancies, and it is well-known that these vacancies in TiO_2 act an n-dopants increasing the material conductivity.[26] Moreover, the electric field applied during the acquisition of the I-V curves can promote further organization of the oxygen vacancies[27] generated by X-ray irradiation, leading to the formation of conductive filaments. However, since C-AFM maps, acquired after writing an irradiation line between the electrodes (Figures 5d and 7c), do not show variations in the TiO_2 surface conductivity even if a higher current is flowing between the two Au contacts with respect to the pristine sample, we can infer that the conductive filaments realized in the TiO_2 crystal

are sub-superficial. This fact seems to suggest that a recombination process between oxygen vacancies induced by irradiation and atmospheric oxygen has taken place in the layers of TiO_2 closest to the surface.[28] This hypothesis is also compatible with the observed time-dependent current change after X-ray irradiation (Figure S3) which shows an initial significant decrease in conductivity, likely arising from the recombination of the surface vacancies with oxygen, and then a very slow variation possibly due to oxygen diffusion processes in the bulk of the TiO_2 single crystal. These phenomena could be potentially exploited to erase the conductive channels by heating the sample in oxygen atmosphere.[29]

3. Conclusions

In this study we have highlighted that two main phenomena occur during X-ray nanobeam irradiation on TiO_2 single crystals. The first one is a volatile resistance change, associated to the presence of photogenerated electrons, which is proportional to the photon flux and is completely reversible upon stopping the irradiation. The second one is a non-volatile local increase in conductivity when an irradiation line is realized between two Au electrodes with a photon flux in the order of 10^{10} photons per second. The non-volatile increase of conductivity can be modulated by varying the beam intensity and the exposure time. This effect can be ascribed to the local generation of oxygen vacancies by the X-ray nanoprobe, which are subsequently ordered by the electric field applied during the acquisition of the I-V curves to form conductive channels. From C-AFM maps we can infer that the conductive filaments realized in the TiO_2 crystal are sub-superficial.

This X-ray nanopatterning (XNP) process is based on the modification of the material oxygen content (and thus of its local electrical properties) induced by the X-ray nanobeam. Up to now this

technique was tested only on non-stoichiometric superconducting oxides, which feature loosely bound oxygen atoms, which can be easily removed, increasing the material resistivity.[11-12] Our results demonstrate that intense synchrotron beams can create oxygen vacancies also in materials with more tightly bound oxygen atoms, indicating the possible extension of the XNP process to the whole class of functional oxide materials. These results can be considered as a crucial step towards establishing the use of X-ray nano-probes as an effective tool for nano-fabrication of oxides, able to locally increase or decrease the material conductivity.

For instance, as the localized presence and migration of oxygen vacancies is the underlying principle in redox-based memristive devices, we envision a new tool for the rational design and production of embedded memories based on memristive devices. With our process we expect to be able to write filaments of oxygen vacancies in defined locations for each device, avoiding the problematic electroforming step, which is performed in the conventional fabrication process. [11-12]

4. Experimental Section

TiO_2 samples and electrical chip preparation. TiO_2 (110) rutile single crystals (10 × 10 × 0.5 mm^3), one side polished, were purchased from CRYSTAL GmbH.

The realization of contacts pattern was performed by laser lithography using Heidelberg Instruments µPG 101 with a write head with 0.9 µm resolution. Two layers of AZ5214 resist were spinned at 3000 rpm for 30 seconds with an intermediate bake at 110 °C for 3 minutes to let the solvent evaporate. The final resist layer thickness, measured by ellipsometry, was about 2 µm. The laser power was optimized for this resist thickness and was consequently set to 6 mW. After resist

development, electrical contacts were deposited by Au physical vapor deposition (thickness 100 nm).

Electrical measurements. For online monitoring, the electrical chips were mounted onto a sample holder compatible with the nanobeam experimental setup and connected with a two-terminal configuration to its contact pads by means of Ag wires 50 μm in diameter. The sample holder was interfaced through coaxial cables to a Keithley 6487 picoammeter/voltage source with high input impedance (10^{11} Ω) and good current resolution (10 fA) with high accuracy (0.3%). The acquisition was controlled by a computer via a GPIB employing a software developed with LabView. The code allows monitoring the electrical properties by selecting two possible configurations: current vs. time recording (applying a constant voltage) or cyclic current-voltage characteristic. For the former approach the sampling rate and the applied bias were fixed at 300 ms and 1 V, respectively, while for the latter a dwell time of 250 ms was set.

X-ray nanobeam irradiation. X-ray irradiation was performed at the long-canted beamline ID16B-NA[30] of the European Synchrotron Radiation Facility (ESRF) in Grenoble, France. The primary beamline optics, which include double white mirror and double crystal monochromator (not employed in this experiment, but used for XAS measurements) are located next to the in-vacuum undulator source to preserve the coherence of the beam.The Kirkpatrick-Baez mirrors, which act as focusing optics, are placed very close to the sample position (165 m far from the undulator source) to obtain a higher degree of demagnification. The horizontal focusing is obtained using a high-β straight section coupled with a horizontal secondary source. The experimental setup includes an optical microscope to visualize the region of interest in the sample, a piezo positioning stage to raster-scan it under the X-ray nanoprobe and an energy dispersive Si drift detector (see Figure 1a) to acquire the XRF signals.

We operated in pink beam mode without double crystal monochromator ($\Delta E/E \approx 10^{-2}$) to obtain a higher photon flux at the sample position. The X-ray nanopatterning procedure was performed at 17.4 keV with beam size (Gaussian-like profile) at the focal plane of 56 × 57 nm^2 (vertical x horizontal), as evaluated by the knife-edge scan method.[31] The photon flux on the sample was varied from 7×10^{10} to 7×10^{8} ph s^{-1} using Si filters of different thicknesses. The XRF maps were collected with a counting time of 0.1 s per point, using a 2 mm Si filter to avoid sample modifications.

Conductive Atomic Force Microscopy. AFM and C-AFM maps were obtained using a Cypher S AFM from Asylum Research (Oxford Instruments group) equipped with the dual gain ORCA cantilever holder. The two gains of the current amplifier of the cantilever holder were respectively 1 nA/V and 1 μA/V. For conductive AFM measurements a HQ:CSC17/AL-BS tip (n-type silicon) from μMasch was employed. During the acquisition of the C-AFM maps the tip was grounded through the current amplifier and the sample was biased at 6 V through a 50 μm Ag wire connected to the main Au electrode.

Scanning Electron Microscopy. SEM images were acquired using an electron microscope Inspect F^{TM} with Field Emission Gun (FEG) from FEI company. Accelerating voltages from 5 to 30 kV were used.

Supporting Information. I-V curves of the TiO_2 crystal acquired before and after 25 minutes of X-ray nanobeam irradiation at the maximum photon flux in a single point; C-AFM current map of the TiO_2 crystal before X-ray nanobeam irradiation.

Acknowledgements

The authors thank the European Synchrotron Radiation Facility (ESRF) for provision of beamtime at the ID16B-NA beamline and for AFM support at the Partnership for Soft Condensed Matter (PSCM). This work has been carried out under project NANO-X jointly approved and funded by University of Torino and Compagnia di San Paolo.

Keywords: maskless X-ray patterning, synchrotron X-ray nanoprobe, conductive AFM, resistive switching, oxygen vacancies.

References

[1] S. P. Hau-Riege, *High-Intensity X-Rays Interaction with Matter*, Wiley-VCH, Weinheim, **2011**.

[2] a) J. M. Holton, *J. Synchrotron Radiat.* **2009**, *16*, 133; b) E. F. Garman, *Acta Crystallogr. Sect. D-Biol. Crystallogr.* **2010**, *66*, 339; c) C. Y. J. Hemonnot, J. Reinhardt, O. Saldanha, J. Patommel, R. Graceffa, B. Weinhausen, M. Burghammer, C. G. Schroer, S. Koster, *ACS Nano* **2016**, *10*, 3553.

[3] G. Martinez-Criado, E. Borfecchia, L. Mino, C. Lamberti, in *Characterization of Semiconductor Heterostructures and Nanostructures (Second Edition)* (Eds.: C. Lamberti, G. Agostini), Elsevier, Amsterdam, **2013**, pp. 361.

[4] a) W. Bras, H. Stanley, *J. Non-Cryst. Solids* **2016**, *451*, 153; b) L. Mino, E. Borfecchia, J. Segura-Ruiz, C. Giannini, G. Martinez-Criado, C. Lamberti, *Reviews of Modern Physics* **2018**, *90*, 025007.

[5] T. Isaji, T. Wakasugi, K. Fukumi, K. Kadono, *Chem. Phys. Lett.* **2012**, *522*, 72.

[6] a) V. Martis, S. Nikitenko, S. Sen, G. Sankar, W. van Beek, Y. Filinchuk, I. Snigireva, W. Bras, *Cryst. Growth Des.* **2011**, *11*, 2858; b) V. I. Feldman, A. A. Zezin, S. S. Abramchuk, E. A. Zezina, *J. Phys. Chem. C* **2013**, *117*, 7286.

[7] V. Kiryukhin, D. Casa, J. P. Hill, B. Keimer, A. Vigliante, Y. Tomioka, Y. Tokura, *Nature* **1997**, *386*, 813.

[8] D. Chernyshov, V. Dyadkin, A. Bosak, *Phase Transit.* **2015**, *88*, 264.

[9] N. Poccia, M. Fratini, A. Ricci, G. Campi, L. Barba, A. Vittorini-Orgeas, G. Bianconi, G. Aeppli, A. Bianconi, *Nature Materials* **2011**, *10*, 733.

[10] a) A. Pagliero, L. Mino, E. Borfecchia, M. Truccato, A. Agostino, L. Pascale, E. Enrico, N. De Leo, C. Lamberti, G. Martinez-Criado, *Nano Lett.* **2014**, *14*, 1583; b) L. Mino, E. Borfecchia, A. Agostino, C. Lamberti, M. Truccato, *Journal of Electron Spectroscopy and Related Phenomena* **2017**, *220*, 69; c) D. Torsello, L. Mino, V. Bonino, A. Agostino, L. Operti, E. Borfecchia, E. Vittone, C. Lamberti, M. Truccato, *Phys. Rev. Mater.* **2018**, *2*, 8.

[11] M. Truccato, A. Agostino, E. Borfecchia, L. Mino, E. Carat, A. Pagliero, N. Adhlakha, L. Pascale, L. Operti, E. Enrico, N. De Leo, M. Fretto, G. Martinez-Criado, C. Lamberti, *Nano Lett.* **2016**, *16*, 1669.

[12] L. Mino, V. Bonino, A. Agostino, C. Prestipino, E. Borfecchia, C. Lamberti, L. Operti, M. Fretto, N. De Leo, M. Truccato, *Sci Rep* **2017**, *7*, 9.

[13] R. Jany, C. Richter, C. Woltmann, G. Pfanzelt, B. Forg, M. Rommel, T. Reindl, U. Waizmann, J. Weis, J. A. Mundy, D. A. Muller, H. Boschker, J. Mannhart, *Adv. Mater. Interfaces* **2014**, *1*, 7.

[14] H. T. Zhang, L. Guo, G. Stone, L. Zhang, Y. X. Zheng, E. Freeman, D. W. Keefer, S. Chaudhuri, H. Paik, J. A. Moyer, M. Barth, D. G. Schlom, J. V. Badding, S. Datta, V. Gopalan, R. Engel-Herbert, *Adv. Funct. Mater.* **2016**, *26*, 6612.

[15] S. H. Chang, J. Kim, C. Phatak, K. D'Aquila, S. K. Kim, J. Kim, S. J. Song, C. S. Hwang, J. A. Eastman, J. W. Freeland, S. Hong, *ACS Nano* **2014**, *8*, 1584.

[16] R. Waser, R. Dittmann, G. Staikov, K. Szot, *Adv. Mater.* **2009**, *21*, 2632.

[17] B. Mohammad, M. A. Jaoude, V. Kumar, D. M. Al Homouz, H. Abu Nahla, M. Al-Qutayri, N. Christoforou, *Nanotechnol. Rev.* **2016**, *5*, 311.

[18] a) S. Kim, S. Choi, W. Lu, *ACS Nano* **2014**, *8*, 2369; b) S. Menzel, U. Bottger, M. Wimmer, M. Salinga, *Adv. Funct. Mater.* **2015**, *25*, 6306.

[19] a) C. Baeumer, R. Valenta, C. Schmitz, A. Locatelli, T. O. Mentes, S. P. Rogers, A. Sala, N. Raab, S. Nemsak, M. Shim, C. M. Schneider, S. Menzel, R. Waser, R. Dittmann, *ACS Nano* **2017**, *11*, 6921; b) J. H. Yoon, J. M. Zhang, X. C. Ren, Z. R. Wang, H. Q. Wu, Z. Y. Li, M. Barnell, Q. Wu, L. J. Lauhon, Q. F. Xia, J. J. Yang, *Adv. Funct. Mater.* **2017**, *27*, 9.

[20] a) N. Szydlo, R. Poirier, *J. Appl. Phys.* **1980**, *51*, 3310; b) Z. Zhang, J. T. Yates, *Chem. Rev.* **2012**, *112*, 5520; c) M. S. Arshad, S. Trafela, K. Z. Rozman, J. Kovac, P. Djinovic, A. Pintar, *J. Mater. Chem. C* **2017**, *5*, 10509.

[21] a) W. X. Dai, X. X. Wang, P. Liu, Y. M. Xu, G. S. Li, X. Z. Fu, *J. Phys. Chem. B* **2006**, *110*, 13470; b) H. L. Xue, X. Z. Kong, Z. R. Liu, C. X. Liu, J. R. Zhou, W. Y. Chen, S. P. Ruan, Q. Xu, *Appl. Phys. Lett.* **2007**, *90*, 3.

[22] M. Garganourakis, V. Scagnoli, S. W. Huang, U. Staub, H. Wadati, M. Nakamura, V. A. Guzenko, M. Kawasaki, Y. Tokura, *Phys. Rev. Lett.* **2012**, *109*, 5.

[23] L. Mino, G. Agostini, E. Borfecchia, D. Gianolio, A. Piovano, E. Gallo, C. Lamberti, *J. Phys. D-Appl. Phys.* **2013**, *46*, 72.

[24] J. Cazaux, *J. Microsc.-Oxf.* **1997**, *188*, 106.

[25] a) M. L. Knotek, P. J. Feibelman, *Surf Sci* **1979**, *90*, 78; b) S. Tanaka, K. Mase, S. Nagaoka, *Surf Sci* **2004**, *572*, 43.

[26] a) P. Knauth, H. L. Tuller, *J. Appl. Phys.* **1999**, *85*, 897; b) M. K. Nowotny, T. Bak, J. Nowotny, *J. Phys. Chem. B* **2006**, *110*, 16270.

[27] a) B. Prasad, W. R. Zhang, J. Jian, H. Y. Wang, M. G. Blamire, *Adv. Mater.* **2015**, *27*, 3079; b) T. Fix, E. M. Choi, J. W. A. Robinson, S. B. Lee, A. P. Chen, B. Prasad, H. Y. Wang, M. G. Blamire, J. L. MacManus-Driscoll, *Nano Lett.* **2013**, *13*, 5886.

[28] a) C. L. Pang, R. Lindsay, G. Thornton, *Chem. Soc. Rev.* **2008**, *37*, 2328; b) L. Mino, G. Spoto, S. Bordiga, A. Zecchina, *J. Phys. Chem. C* **2012**, *116*, 17008; c) L. Mino, G. Spoto, S. Bordiga, A. Zecchina, *J. Phys. Chem. C* **2013**, *117*, 11186.

[29] M. H. Kim, S. B. Baek, U. Paik, S. Nam, J. D. Byun, *J. Korean Phys. Soc.* **1998**, *32*, S1127.

[30] G. Martinez-Criado, J. Villanova, R. Tucoulou, D. Salomon, J. P. Suuronen, S. Laboure, C. Guilloud, V. Valls, R. Barrett, E. Gagliardini, Y. Dabin, R. Baker, S. Bohic, C. Cohen, J. Morse, *J. Synchrotron Radiat.* **2016**, *23*, 344.
[31] A. Takeuchi, Y. Suzuki, K. Uesugi, *Jpn. J. Appl. Phys.* **2015**, *54*, 092401.